ITC 4/54
Information Technology and Control
Vol. 54 / No. 4/ 2025
pp. 1383-1407
DOI 10.5755/j01.itc.54.4.41193

BioDiag-Net: Dynamic Multisite Graph Convolutional Network for Computer-Aided ASD Diagnosis with Biomarker Visualization

Received 2025/04/15 | Accepted after revision 2025/08/11

HOW TO CITE: Yu, B., Li, Y., Ren, Z., Pan, J. (2025). BioDiag-Net: Dynamic Multisite Graph Convolutional Network for Computer-Aided ASD Diagnosis with Biomarker Visualization. *Information Technology and Control*, 54(4), 1383-1407. https://doi.org/10.5755/j01.itc.54.4.41193

BioDiag-Net: Dynamic Multisite Graph Convolutional Network for Computer-Aided ASD Diagnosis with Biomarker Visualization

Bo Yu*, Yue Li, Zehua Ren, Jingqi Pan
School of Computer Science and Technology, Harbin University of Science and Technology, Harbin 150080, China

Corresponding author: lifuji2025@163.com; yubo@hrbust.edu.cn

Autism spectrum disorder (ASD) is characterized by significant social communication deficits and restricted/repetitive behaviors. Traditional behavioral diagnostics for ASD primarily rely on subjective clinical observations and standardized behavioral assessments, which face several limitations. These methods often lack objective biological markers, are susceptible to observer bias, and may not fully capture the complex neurobiological underpinnings of ASD. To address these challenges, we propose BioDiag-Net, a deep learning-based dynamic graph convolutional network that integrates spatial brain topology with resting-state fMRI (rs-fMRI) functional connectivity. The architecture adaptively fuses whole-brain features with default mode network (DMN) dynamics through mutual information-driven selection, effectively suppressing noise while preserving neurobiologically relevant patterns. Evaluated on the ABIDE I dataset (1,035 multisite rs-fMRI scans), BioDiag-Net achieves 83.48% accuracy in ASD classification, capturing both global network reorganization and localized DMN aberrations. Biomarker visualization enables interpretable neuroimaging diagnosis, revealing neurophysiological substrates, providing interpretable diagnostic evidence while demonstrating transfer potential for cross-disorder neuroimaging analysis. This work bridges computational neuroscience with clinical practice, advancing personalized psychiatric diagnostics.

KEYWORDS: Autism spectrum disorder, Deep learning, Default mode network, Neuroimaging diagnosis, Resting-State fMRI

1. Introduction

Autism spectrum disorders (ASD) are pervasive neurodevelopmental conditions that impact both children and adults, characterized by persistent deficits in verbal communication, social interaction, and behavioral patterns, among which research pointed out that the typical symptoms of autism include social communication and interaction deficits and perceptual abnormalities [22], which are demonstrated in Figure 1, and proposed a self-organizing criticality approach for understanding crisis behavior in ASD. In current clinical practice, behavioral observations coupled with standardized instruments such as the Autism Diagnostic Observation Schedule (ADOS) and Autism Diagnostic Interview-Revised (ADI-R) remain cornerstone methods for ASD diagnosis. While these tools facilitate symptom identification through systematic evaluation of social reciprocity, linguistic development, and stereotyped behaviors, several critical limitations persist.

Figure 1
Typical symptoms of ASD.

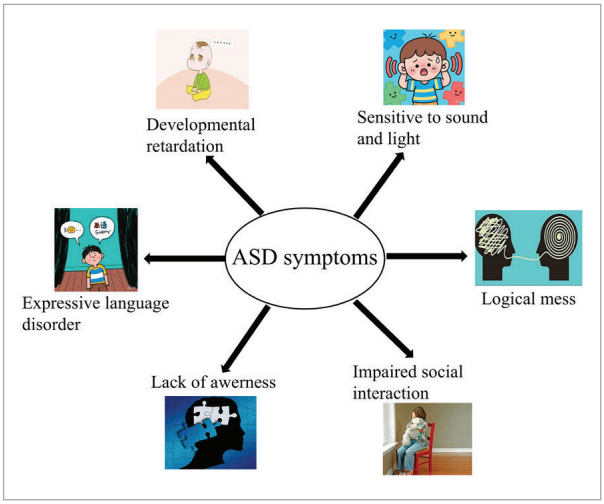

First, the lack of an explanation of the neural mechanisms underlying the behaviors prevents a more thorough biological basis for the diagnosis; second, due to differences in clinical presentation between children and adults, standardized diagnostic tools are difficult to apply across age groups; and third, there is a greater reliance on the subjective judgment of the assessor, and since consistency varies widely among assessors, they are susceptible to large diagnostic errors. As a result, the shortcomings of conventional techniques force us to look for more reliable and objective biomarkers for autism diagnosis, opening up a new avenue for early screening and precise subtyping.

The continuous evolution of neuroimaging technology has propelled brain imaging modalities, particularly functional magnetic resonance imaging (fMRI), to the forefront of investigating neurobiological substrates of ASD. This technological progress drives contemporary neuroscience to prioritize developing objective neuroimaging analytics for early ASD detection. As a non-invasive technique, fMRI leverages the blood oxygenation level-dependent (BOLD) effect, which infers neural activity through hemodynamic changes in oxygenated blood flow during both task-evoked and resting-state conditions [34]. Its predominant application in ASD research stems from the capability to detect characteristic functional connectivity anomalies within large-scale brain networks.

Most early studies employed functional connectivity (FC) analyses using conventional machine learning frameworks. For instance, Chen et al. [3] evaluated three algorithms—Random Forest (RF), Support Vector Machine (SVM), and Naive Bayes (NB). The findings indicate that the random forest approach is thought to be the most effective technique for neuroimaging data mining in this small sample size investigation. Building on this, Kazeminejad et al. [13] proposed a graph-theoretical SVM classifier leveraging 816 rs-fMRI scans from the ABIDE I repository, achieving 95% accuracy (95% CI: 92-97%) in adults >30 years through 10-fold cross-validation. However, it has not yet attained the anticipated level of applicability in the child and adolescent populations. 240 adolescents with ASD and 128 healthy controls were chosen from six ABIDE international sites [5]. A whole-brain functional connectivity network was built using the Slow-5 (0.01-0.027 Hz) and Slow-4 (0.027-0.073 Hz) frequency bands as the classification features. A support vector machine was used to classify the data, and the classification accuracy was 79.17%. It is difficult to capture the deep patterns and complex relationships in high-dimensional data, and machine learning models have

poor interpretability of decision boundaries and internal mechanisms, particularly in the medical field where the basis for model decisions needs to be explained.

These machine learning methods, despite their strong classification ability, are typically sensitive to the quality and quantity of the input data, and when dealing with complex brain functional connectivity data, they have limited ability to model nonlinear relationships. Deep learning techniques, on the other hand, demonstrate significant advantages in processing high-dimensional data by using multilayer nonlinear transformations to capture intricate patterns in the data. Additionally, the performance of deep learning techniques tends to improve with increasing data volumes, which makes them a promising approach for processing large-scale brain imaging data. For example, some studies using non-graph convolutional networks, Almuqhim et al. [1] developed a deep learning model that uses a sparse autoencoder to refine the classifier and enhance feature extraction based on classifier errors and reconstructed data discrepancies. To improve the model's adaptability to small sample data, Zhang et al. [31] employed a denoising autoencoder with Gaussian noise for robust feature extraction. Subsequently, it used a shared-weight mechanism to initialize the features learned by the autoencoder into the convolutional layer weights of a convolutional neural network (CNN). Although these studies employ proof-of-concept autoencoders for the task, the spatial structure information across brain regions is not preserved because the feature representations of fMRI images are transformed into vectors during feature extraction.

Here are some studies that use graph convolutional networks. Ma et al. [18] overcame the traditional single-atlas limitation by constructing a multimodal fusion template through computing inter-regional spatial overlap, thereby capturing the synergistic features of whole-brain functional connectivity. The model implemented a graph convolutional network (GCN) for feature extraction from the fused dynamic network, achieving 10-fold cross-validation accuracy of 75.7% on the ABIDE dataset. However, the multi-graph fusion strategy demonstrates limitations, including sensitivity to noise and data heterogeneity. The residual graph transformer for autism spectrum disorder prediction proposed in [25] integrated the residual connection mechanism. Its dual-channel architecture simultaneously models the temporal dependence and spatial correlation of functional connectivity (FC) matrices, optimally balancing computational complexity and feature dimensionality through adaptive sparsification. Wen et al. [27] adopted a multitask collaborative training strategy to jointly optimize graph structure learning and feature embedding. This approach not only enhances classification performance on the ABIDE dataset but also achieves 71.2% cross-dataset validation accuracy on the ADNI (Alzheimer's disease dataset), demonstrating cross-disease generalization. Nevertheless, these studies demonstrate limitations including constrained global structural perception and interpretability constraints in feature extraction.

In response to the critical analysis of existing neuroimaging-based diagnostic studies for ASD, we identify three key challenges. First, traditional graph models treat brain regions as topology-independent nodes, disregarding anatomical location impacts on functional connectivity (FC) patterns (e.g., the strong connectivity tendency of neighboring brain regions), thus failing to distinguish local versus long-range connectivity abnormalities crucial for ASD diagnosis.

Second, existing methods rely on average fusion or fixed weights for multiscale features (whole-brain vs. specific-network), which lacking adaptive mechanisms to capture hierarchical network interactions, leading to ineffective utilization of complementary features and noise-dominated biomarkers.

Finally, conventional feature selection methods based on statistical tests or L1 regularization fail to consider higher-order interactions between features. This oversight can cause the model to be interfered with by numerous irrelevant connections, retain redundant connections (particularly those strong connections not specific to ASD diagnosis), and lead to model overfitting due to redundant information in high-dimensional features. Moreover, key weakly connected biomarkers may be filtered out by these conventional methods.

To address these limitations, we propose BioDiag-Net, a novel GCN framework with three key innovations.

1 A spatial prior injection module (SPI) is constructed using learnable multi-frequency sinusoidal cosine coding, differing from fixed-position coding. This introduces spatial prior information capturing positional relationships at various spatial scales, enabling the model to recognize brain-region anatomical relationships. This is a key capability absent in previous ASD studies using coordinate-independent graph networks.

2 A Cross-Channel Interaction Fusion Module (CCIF) is introduced to adaptively and dynamically fuse whole-brain functional connectivity network features with DMN features. Through context-aware weight assignment, it highlights disease-related connectivity patterns and introduces a dynamic weighting mechanism based on channel attention. Unlike common cascade or additive fusion, this enables automatic feature-importance adjustment per sample, preventing critical pathology information from being masked by noise. It also avoids losing brain-wide compensatory connectivity-change information when not focusing on critical DMN abnormal connections.

3 A node screening method (GFS-MI) based on graph feature selection with mutual-information maximization is used to identify neurobiologically significant biomarkers. By information-theoretic criteria, this method screens biomarkers highly correlated with ASD labels, enhancing model interpretability and reducing overfitting risks. Performed in the graph domain, it considers both node features and topology, unlike traditional threshold-based feature linkage selection methods.

2. Methodology

2.1. Framework Overview

In this study, we propose an efficient model leveraging resting-state functional magnetic resonance imaging (rs-fMRI) data to identify biomarkers linked to autism and achieve accurate diagnosis. As illustrated in Figure 2, the BioDiag-Net framework comprises three core components. The workflow is as follows: Initially, the blood oxygen level-dependent (BOLD) time series of each region-of-interest (ROI) are extracted from rs-fMRI data to construct nodes and functional connectivity matrices, followed by node feature extraction. Subsequently, the cross-channel interaction fusion module acts as a feature aggregator along the channel dimension, employing global average pooling to quantify the global feature distribution across channels and generates dynamic weights to adjust each channel's contri-

Figure 2

Overview of the BioDiag-Net model. The ROI classification based on CC200 Atlas is performed to extract the average time series of, and then the time series are input to our proposed model to perform a series of operational transformations and finally passed through the MLP in order to obtain the prediction results.

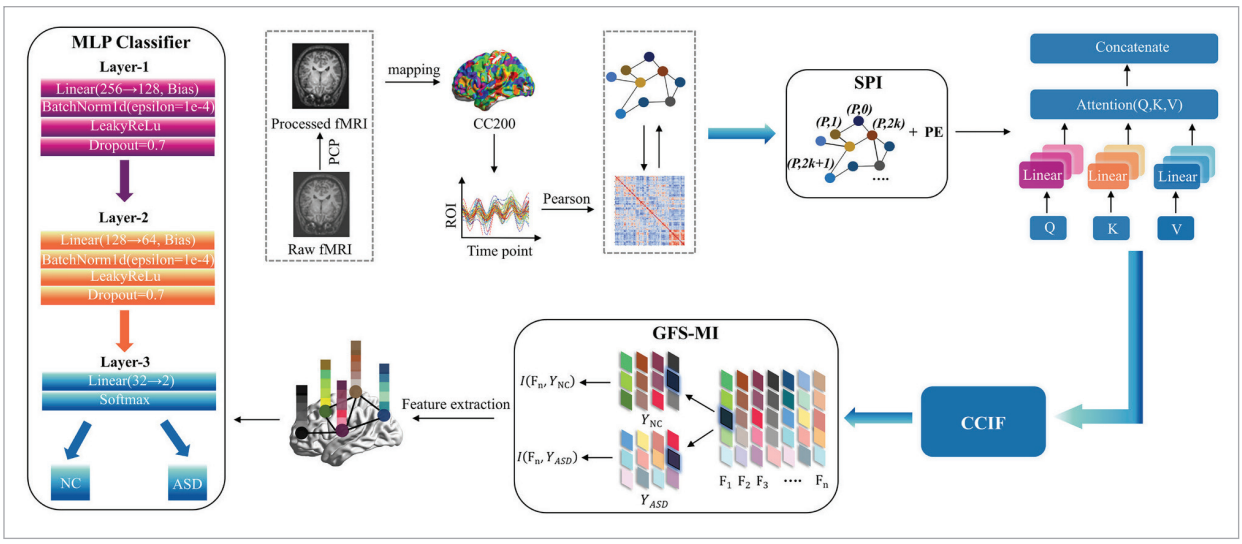

bution, thereby enhancing feature representation capability of GCN. Finally, a node selection method based on graph feature selection and mutual information maximization is applied to filter out the most discriminative features from the complex feature set. These selected features are then fed into a classifier to predict and diagnose ASD, providing further empirical evidence for existing conclusions about brain regions strongly associated with ASD.

2.2. Data Processing and Feature Extraction

2.2.1. Pearson Correlation

Previous research has established that specific functional subnetworks, such as the default mode network (DMN), play a pivotal role in ASD pathogenesis [20].

According to Figure 3, it can be observed that the surface-to-volume ratios of ROIs for CC200 atlas are more reflective of the boundaries of ROIs than the other three atlases, and the anatomical accuracy is higher, which can be used to locate DMN more accurately and is closer to the topological characteristics of the real functional network. Therefore, in this study, we employ the CC200 atlas parcellating the brain into 200 regions (each corresponding to a graph node). Spatial coordinates of each brain region are mapped from fMRI data to their anatomical labels.

Through this mapping, DMN-related regions including the medial prefrontal cortex (mPFC), posterior cingulate cortex (PCC), and precuneus are identified. The BOLD signal time series are derived by averaging all voxel-wise time courses within each region, representing functional activity dynamics across temporal vector T (scan duration). The extraction pipeline proceed is presented in Equation (1) and Equation (2):

$$X_i = [X_i(t_1), X_i(t_2), ..., X_i(t_T)], \quad (1)$$

$$X_j = [X_j(t_1), X_j(t_2), ..., X_j(t_T)]. \quad (2)$$

In Equation (1) and Equation (2), $X_i \in R^{n\times t}$ presents the time series of the entire brain region i, $X_j \in R^{m\times t}$ denotes the time series of DMN-related region j, n is the total number of ROIs, m is the number of DMN-related regions, and t represents distinct time points.

Next, we compute the pairwise Pearson correlation coefficients to quantify the connectivity between all brain nodes. Specifically, the correlation $A_{aa'}$ between node a and node a′ is calculated using the following Equation (3):

$$A_{aa'} = \frac{\sum_{t=1}^{T}\left(X_a(t)-\bar{X}_a\right)\left(X_{a'}(t)-\bar{X}_{a'}\right)}{\sqrt{\sum_{t=1}^{T}\left(X_a(t)-\bar{X}_a\right)^2\sum_{t=1}^{T}\left(X_{a'}(t)-\bar{X}_{a'}\right)^2}}. \quad (3)$$

After calculating the pairwise correlations between all brain regions and the DMN-related brain regions, the results are combined into a symmetric matrix, whose structures are presented in Equation (4) and Equation (5), respectively.

$$A_{whole} = \begin{bmatrix} A_{11} & A_{12} & \cdots & A_{1n} \\ A_{21} & A_{22} & \cdots & A_{2n} \\ \vdots & \vdots & \ddots & \vdots \\ A_{n1} & A_{n2} & \cdots & A_{nn} \end{bmatrix}, \quad (4)$$

$$A_{dmn} = \begin{bmatrix} A_{11} & A_{12} & \cdots & A_{1m} \\ A_{21} & A_{22} & \cdots & A_{2m} \\ \vdots & \vdots & \ddots & \vdots \\ A_{m1} & A_{m2} & \cdots & A_{mm} \end{bmatrix}. \quad (5)$$

Figure 3
Comparison of surface-to-volume ratios of ROIs for CC200 atlas (a), AAL atlas (b), EZ atlas (c) and HO atlas (d).

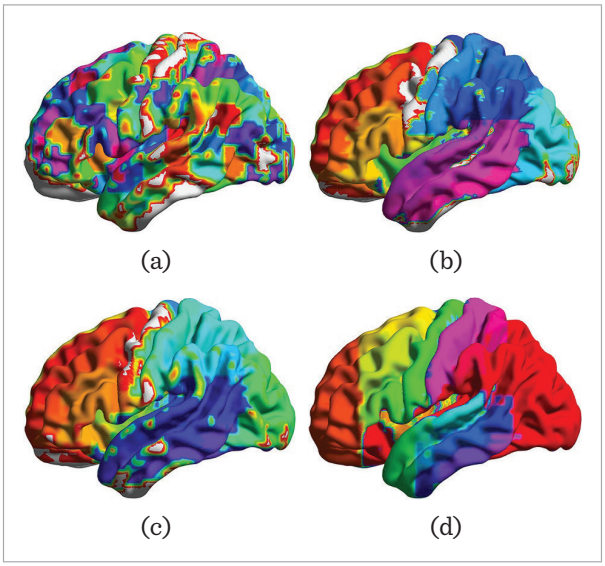

In Equations (4)-(5), $A_{whole} \in R^{n\times n}$ is the whole-brain connectivity matrix, $A_{dmn} \in R^{m\times m}$ is DMN-specific functional connectivity matrix, $X_{\mathrm{a}}(t)$ and $X_{\mathrm{a}'}(t)$ are the BOLD signal values of brain regions a and a′ at time point t, and $\overline{X}_{\mathrm{a}}$ and $\overline{X}_{\mathrm{a}'}$ are the mean values of their respective time series.

2.2.2. Spatial Prior Injection

In ASD diagnosis tasks, the functional connectivity matrix intrinsically represents a graph structure. Inspired by [23], we introduce a learnable positional embedding $p(p \in [0, 1, 2, \ldots, \mathrm{n}-1])$ prior to feature extraction. This module aims to inject spatial priors into each node, enabling the model to comprehend the spatial layout of brain regions and improve its ability to capture interaction patterns between regions. Positional encoding transforms the spatial coordinates of nodes into vectors and integrates them into the node features, endowing each node with a unique representation that combines intrinsic features and spatial localization.

In this process, we utilize sine and cosine functions to generate positional encodings. These functions leverage the periodic nature of spatial information, encoding distinct dimensions via frequency modulation. This design ensures high discriminability between positional encodings, mitigating redundancy that would arise from uniform frequency encoding. By assigning dimension-specific frequencies, the encodings preserve spatial topology and quantify node proximity.

Through element-wise addition, each input vector incorporates positional information, allowing the model to infer sequential relationships among elements without relying on recurrent structures. Let p denote the relative position of the p-th element in the input sequence, and d represents the feature dimension. The positional encoding process is illustrated in Equation (6) and Equation (7).

$$PE(p, 2k) = \sin\left(\frac{p}{10000^{\frac{2k}{d}}}\right), \tag{6}$$

$$PE(p, 2k+1) = \cos\left(\frac{p}{10000^{\frac{2k}{d}}}\right). \tag{7}$$

In Equations (6)-(7), k is the index of the feature dimension, $k \in [0, 1, 2, \ldots, d-1]$. Here, sine functions encode even-indexed dimensions, while cosine functions encode odd-indexed dimensions. This strategy ensures that different dimensions exhibit distinct frequency patterns, enabling the model to distinguish elements at varying positions even for long sequences.

The resulting positional encoding matrix $PE \in R^{n\times d}$ has a shape of $n \times d$, where each row corresponds to the positional encoding vector for position p. The original input sequence is adjusted with positional embeddings as shown in Equation (8):

$$X' = X + PE\ . \tag{8}$$

In Equation (8), the original input feature matrix $X \in R^{n\times d}$, containing n nodes (e.g., brain regions) with d-dimensional features, is adjusted through positional embedding. The position encoding matrix $PE \in R^{n\times d}$, which encodes the k-th dimensional information of position p via learnable embeddings, is computed to provide positional information for each node. The output matrix, denoted as X', represents the integration of the original features and positional information. The addition operation is performed element-wise, ensuring that each input vector retains both its intrinsic features and positional awareness. This integration enables the model to leverage spatial relationships without relying on explicit recurrence.

Although brain connectomes are not inherently sequential, we treat ROIs as ordered sequences based on their anatomical positions in the CC200 template. This allows the model to preserve spatial relationships between brain regions. Position encoding is generated by iterating over all nodes and feature dimensions, with each value computed in constant time, leading to a time and space complexity of $O(n \times d)$, it requires storing the position encoding matrix PE and the encoded feature matrix. The encoded features are then integrated into the functional connectivity matrix to enhance spatial awareness. This approach is particularly effective for brain imaging data with explicit spatial structures. In ASD diagnosis, it enables the model to better capture inter-regional spatial dependencies, improving diagnostic accuracy. With linear computational complexity,

this method efficiently handles large-scale datasets and is well-suited for real-time clinical applications.

2.2.3. MSA-Based Feature Extraction

When modeling relationships between brain regions, relying solely on local temporal or spatial information proves insufficient for capturing complex global structures, as these interactions extend beyond local domains and exhibit pronounced long-range dependencies. Functional connectivity in ASD patients may span multiple brain regions, particularly within networks such as DMN, a pattern frequently overlooked by conventional feature extraction methods. To address this limitation, we implement multi-head self-attention (MSA) to compute relationships between elements in the input sequence, effectively capturing long-range dependencies.

The MSA framework leverages queries (Q), keys (K), and values (V) to dynamically compute attention weights, enabling the identification of critical inter-regional relationships and establishing biologically meaningful associations. Specifically, Q represents the dynamic activity state of a given brain region, captured through temporal features of its time series, and reflects its momentary activation pattern. K encodes the static topological properties of other brain regions in the functional connectivity graph, serving to indicate their potential influence on the target region. Meanwhile, V carries the functional signal intensity of the target region, typically derived from BOLD signals, and directly contributes to the computation of the final attention weights. Specifically, taking the DMN of patients with ASD as an example, this network often shows a phenomenon of weakened long-term connections (such as the separation between the anterior cingulate cortex and the posterior cingulate cortex) and enhanced local connections. Within the proposed architecture, Q captures the transient activation states of key nodes within the DMN, such as the medial prefrontal cortex. K encodes the potential modulatory influence of other regions, such as the precuneus, on these DMN nodes. Finally, V quantifies the functional signal strength of the target region, such as the posterior cingulate cortex, thereby reflecting its impact on the overall network dynamics.

Within ASD-related functional connectivity networks, the relative importance of connection strengths and topological configurations varies across brain regions. By deploying MSA with parallel computation across multiple attention heads, the model simultaneously extracts diverse relational patterns from heterogeneous perspectives, adaptively adjusts feature weights, and prioritizes clinically relevant brain regions and their connectivity profiles.

The MSA layer at layer l receives the output feature matrix from the preceding layer (l–1), denoted as $X'^{(l\text{-}1)} \in R^{n\times d}$, is received as input. Here, n represents the number of nodes (the number of brain regions in fMRI data), and d represents the feature dimension of each node. The rationale for using $X'^{(l\text{-}1)}$ as the input lies in the hierarchical feature extraction mechanism commonly employed in deep learning. Typically, the input to layer l is based on the output from layer (l–1). This layer-by-layer propagation enables the model to progressively aggregate both local and global relationships, thereby optimizing the representation of nodes.

For each attention head h in layer l, the input $X'^{(l\text{-}1)}$ is projected into three distinct vectors—Q, K, and V, via trainable weight matrices $W_Q^{(\mathrm{h})} \in R^{d_k\times d}$, $W_K^{(\mathrm{h})} \in R^{d_k\times d}$ and $W_V^{(\mathrm{h})} \in R^{d_k\times d}$ respectively. Here, d_k represents the dimensionality of the query and key vectors for each head. The projection process is shown in Equations (9)-(11).

$$Q^{(\mathrm{h})} = \mathrm{X}'^{(1-1)} W_Q^{(\mathrm{h})}, \tag{9}$$

$$K^{(\mathrm{h})} = \mathrm{X}'^{(1-1)} W_K^{(\mathrm{h})}, \tag{10}$$

$$V^{(\mathrm{h})} = \mathrm{X}'^{(1-1)} W_V^{(\mathrm{h})}. \tag{11}$$

Next, the dot product is used to measure similarity between Q and K, followed by a Softmax operation to normalize the similarity scores into attention weights (summing to 1). The single-head attention computation is defined as Equation (12):

$$Att^{(h)}(Q,K,V) = \mathrm{Softmax}\left(\frac{Q^{(h)}K^{(h)T}}{\sqrt{d_k}}\right)V^{(h)}. \tag{12}$$

In Equation (12), $\sqrt{d_k}$ is a scaling factor to mitigate gradient instability caused by large dot product magnitudes. The multi-head mechanism operates

through parallel computation, where the formula for each attention head *i* that extracts heterogeneous relational patterns from the input space is represented by Equation (13):

$$h_i = Att^{(i)}(X'^{(l-1)}W_Q^{(i)}, X'^{(l-1)}W_K^{(i)}, X'^{(l-1)}W_V^{(i)}), \quad (13)$$

where h_i represents the output of attention head *i*, the outputs of all *H* attention heads are concatenated along the feature dimension, the process is shown in Equation (14):

$$Concat(h_1, h_2, ..., h_H) = \\ = [Att^{(1)}(Q,K,V), ..., Att^{(H)}(Q,K,V)], \quad (14)$$

where $Concat(h_1, h_2, ..., h_H) \in R^{(H \cdot d_v) \times n}$, d_v is the dimension of each head's value vector, and *n* is the number of nodes.

A learnable linear transformation (weight matrix $W_O \in R^{h_H \cdot d_k \times d}$) projects the concatenated features back to the original dimensionality *d*, the integrated output is formally expressed as Equation (15):

$$Output(Q,K,V) = Concat(h_1, h_2, ..., h_H)W_O. \quad (15)$$

This architectural design enables the model to establish diverse interaction patterns within whole-brain functional connectivity networks while specifically modeling DMN-subnetwork dynamics, ultimately producing clinically interpretable feature representations for downstream analytical tasks.

2.3. The BioDiag-Net Model

2.3.1. Cross-Channel Interaction Fusion

This subsection delineates the integration framework for whole-brain connectivity features $F_{whole} \in R^{d_1 \times n}$ and DMN-specific features $F_{dmn} \in R^{d_2 \times n}$, which encode complementary hierarchical representations of neural organization. The fusion process synergistically combines the global contextual information from whole-brain networks with the subsystem-specific signatures of DMN. By mapping DMN features, the network can focus on functional connectivity patterns in ASD-related brain regions, leveraging biological priors to reveal disease-specific neural substrates. As schematized in Figure 4, we implement cross-hierarchical interaction by first projecting both feature sets into a shared latent space through trainable transformation matrices, as shown in Equation (16), Equation (17), Equation (18), and Equation (19):

$$A_{whole} = W_{proj}^{whole} F_{whole} + b^{whole}, \quad (16)$$

$$W_{proj}^{whole} \in R^{d_1 \times d}, b^{whole} \in R^d, \quad (17)$$

$$A_{dmn} = W_{proj}^{dmn} F_{dmn} + b^{dmn}, \quad (18)$$

$$W_{proj}^{dmn} \in R^{d_2 \times d}, b^{dmn} \in R^d. \quad (19)$$

Given the potentially divergent contributions of whole-brain and DMN features, Zheng et al. [33] investigated dynamic weighted fusion methods in multimodal deep learning, with a focus on integrating functional connectivity data from different brain regions using adaptive weighting mechanisms to improve classification accuracy. Inspired by this approach, we designed a cross-channel interaction fusion module. This module introduces a dynamic weighting coefficient α, which is context-dependent on the input data and tailored to the training objectives. Unlike static averaging methods, α is dynamically updated during training, allowing the model to adaptively adjust the significance of different features according to task requirements. This effectively avoids the potential information loss or error accumulation associated with simple averaging. Distinct from traditional single-modality pooling, we designed a cross-channel interactive pooling layer to capture the correlations among features across different hierarchical levels, as shown in Equation (20):

$$h_{pool} = AvgPool(A_{whole} \oplus A_{dmn}). \quad (20)$$

In Equation (20), $\oplus$ denotes feature concatenation operation, AvgPool(·) is global average pooling, yielding the output h_{pool}. In each training iteration, the network adjusts parameters W_α and b_α based on the input features and the error associated with the target task, and updates them through backpropagation, thereby progressively refining α to better suit the current task. The formula for calculating α can be expressed as Equation (21):

Figure 4

Overview of Cross-Channel Interaction Fusion Module that combines the broad information of the whole brain with the specific patterns of the DMN, GAP (Global Average Pooling) is used to encode the global information efficiently, supports cross-channel interaction modeling, enhances feature representation, and reduces computational complexity.

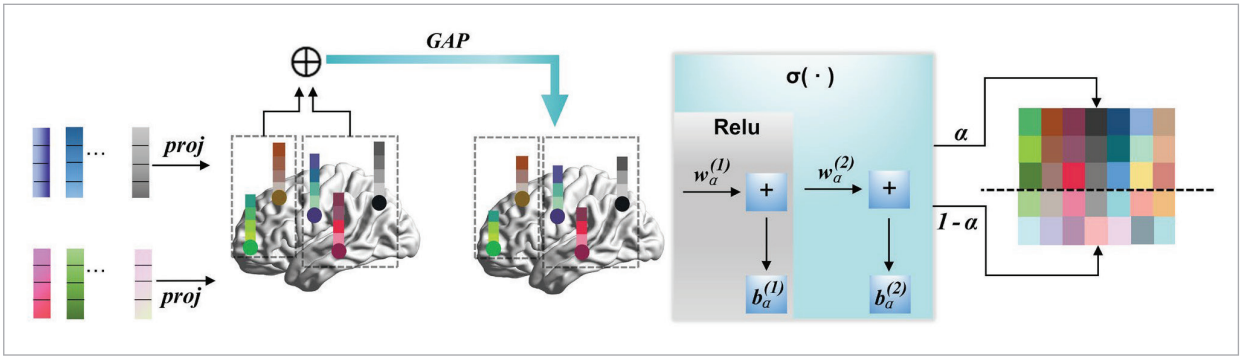

$$\alpha = \sigma(W_{\alpha}^{(2)} \times \mathrm{Re}\,LU\left(W_{\alpha}^{(1)} h_{pool} + b_{\alpha}^{(1)}\right) + b_{\alpha}^{(2)}) . \quad (21)$$

In Equation (21), $W_{\alpha}^{(1)} \in R^{H \times 2D}$, $b_{\alpha}^{(1)} \in R^{H}$, $W_{\alpha}^{(2)} \in R^{1 \times H}$, $b_{\alpha}^{(2)} \in R$ and W_{α} are weight parameters, and b_{α} is the bias term. Subsequently, the weighted sum is activated using the Sigmoid function, which compresses the output values into the range [0, 1].

Weighted fusion of the whole-brain functional connectivity network features and DMN features yields the feature stacking matrix A_{fused}, as shown in Equation (22):

$$A_{fused} = \alpha A_{whole} + (1 - \alpha) A_{dmn} . \quad (22)$$

Here, $A_{fused} \in R^{n \times d}$ is the fused feature matrix (n: number of brain regions, d: feature dimension), while $A_{whole} \in R^{n \times d}$ and $A_{dmn} \in R^{n \times d}$ represent the features of the whole-brain functional connectivity network and the DMN, respectively, $\alpha \in [0,1]$ is the sample-wise adaptive weight vector.

CCIF introduces a context-aware dynamic weighting coefficient α to adaptively balance the contributions of whole-brain and DMN features during training. Unlike static averaging, α is computed via a shallow neural network that applies global average pooling on the concatenated query-key-value embeddings. This design not only ensures that the model focuses more on task-relevant features but also avoids introducing excessive computational overhead, thereby enhancing the flexibility and adaptability of feature fusion while maintaining model efficiency.

The CCIF module performs projection and weighted fusion through matrix multiplication and element-wise operations, with a time and space complexity of $O(n \times d)$, linear in the size of the feature matrix. It stores latent features, shared representations, and fused outputs. Functionally, CCIF integrates features from different brain networks, which is essential for diagnosing complex disorders like ASD. Through dynamic weight adjustment, the model enhances sensitivity to disease-relevant features. For instance, in multicenter studies, CCIF mitigates site-specific variations by adaptively recalibrating feature weights, thereby improving generalizability. Its linear complexity also makes it suitable for deployment in resource-constrained environments, such as mobile or tele-diagnostic systems.

2.3.2. Graph Feature Selection and Mutual

Through this step, we obtain a fused feature matrix. Next, we design a node screening method based on graph feature selection and mutual information maximization to calculate the mutual information between each node feature $F_c = A_{fused}[c,:]$, the target label is represented as $Y \in \{Y_{Control}, Y_{ASD}\}$, where $Y_{Control} = 0$, $Y_{ASD} = 1$. Then, based on the results of mutual information calculation, we filter out features that have weak relevance to the label and retain those that are closely related to the label and have high predictive value for the target task. This not only reduces the computational complexity of the model but also enhances its generalization ability. To estimate mutual information, we use the k-nearest neighbors (k-NN) method, a non-parametric

method for estimating entropy and joint entropy from continuous data. The k-NN method is chosen for its simplicity and effectiveness in estimating mutual information. For each feature F_c, we use the k-NN method to estimate its entropy $H(F_c)$, which can be obtained according to Equation (23):

$$H(F_c) \approx \psi(k) + \log(n) + \mathrm{E}\left[\log\left(\frac{k}{n \cdot V_d \cdot r_k(F_c)^d}\right)\right], \quad (23)$$

where $\psi(k)$ is the digamma function for bias correction, n is the total number of brain region nodes, V_d is a normalization constant for adjusting distance measurements in different dimensional feature spaces, $r_k(F_c)$ is the distance from sample point F_c to its k-th nearest neighbor, E[·] denotes the expectation over all samples, and d is the dimension of the feature space. For the joint feature (F_c, Y), we use the k-NN method to estimate its joint entropy $H(F_c, Y)$, as shown in Equation (24):

$$H(F_c, Y) \approx \psi(k) + \log(n) + \\ + \mathrm{E}\left[\log\left(\frac{k}{n \cdot V_{d+1} \cdot r_k(F_c, Y)^{d+1}}\right)\right], \quad (24)$$

where d+1 is the dimension of the joint feature space (the space constituted by feature F_c and label Y), and V_{d+1} is a normalization constant for adjusting distance measurements in the joint feature space. The formula for calculating the mutual information $I(F_c, Y)$ can be expressed as Equation (25):

$$I(F_c, Y) = H(F_c) + H(Y) - H(F_c, Y). \quad (25)$$

In Equation (25), $H(F_c)$ is the entropy of the feature F_c, which represents the self-uncertainty of the feature $H(Y)$ is the entropy of the label Y, which represents the self-uncertainty of the label, $H(F_c, Y)$ is the joint entropy of the feature F_c and the label Y, which represents the common uncertainty between the feature and the label, the greater the mutual information between the feature and the label, the greater the contribution of the feature to the label prediction, based on the results of the calculation of the mutual information, we can select the feature with higher relevance to the label.

Usually, features with higher mutual information values are selected as inputs, and those with weaker relationships with labels are ignored. Then a new feature matrix A_{fused} is constructed, which contains only the selected features with high mutual information. Next, the features need to be converted into a graph structure representation by calculating the similarity matrix between the nodes through the inner product of the feature matrix as the adjacency matrix A_{sim} of the graph, as shown in Equation (26):

$$A_{sim} = \frac{A_{fused} A_{fused}^T}{\| A_{fused} \|^2}. \quad (26)$$

In Equation (26), A_{fused}^T is the transpose of the feature matrix, which calculates the similarity between nodes, through which the adjacency matrix of the graph is constructed, and A_{sim} is normalized in order to eliminate the differences in feature scales.

Next, according to Equation (27), the identity matrix I is added to the adjacency matrix, effectively adding a self-loop (with weight 1) to each node. This operation ensures that each node retains its original features during information aggregation, rather than relying solely on its neighboring nodes, thus achieving self-connection:

$$\tilde{A}_{sim} = A_{sim} + I. \quad (27)$$

The process of summing the similarity weights of all neighbors y of node x in the adjacency matrix $\tilde{A}_{sim}$ to obtain the degree matrix $\tilde{D}$ is shown in Equation (28):

$$\tilde{D}_{xx} = \sum_y \tilde{A}_{sim_{xy}}, \quad (28)$$

Here, $\tilde{D}_{xx}$ represents the diagonal element of the degree matrix $\tilde{D}$ at row x and column x, which is the degree of node x (the sum of edges connected to the node), $\sum_y$ denotes the summation over all neighbors y of node x, and $\tilde{A}_{sim_{xy}}$ is the element of the adjacency matrix $\tilde{A}_{sim}$ at row x and column y. The final step of constructing the similarity matrix via node feature inner products, adding self-connections, and performing symmetric normalization to obtain the matrix is shown in Equation (29):

$$\hat{A} = \tilde{D}^{-1/2} \tilde{A}_{sim} \tilde{D}^{-1/2}, \quad (29)$$

where $\tilde{D}^{-1/2}$ is obtained by taking the inverse square root of the diagonal elements of the degree matrix $\tilde{D}$.

In the feature selection stage, we employ the k-NN method to estimate mutual information between node features and target labels. Unlike kernel density estimation, k-NN is a non-parametric approach that does not assume specific data distributions, making it more suitable for diverse brain imaging data. MI computation involves sorting operations with a time complexity of $O(n \times d \times \log n)$, while similarity matrix construction and normalization contribute $O(n^2)$. The overall space complexity is $O(n \times d)$. The GFS-MI method effectively identifies and retains features highly correlated with autism labels, improving both diagnostic performance and model interpretability. For instance, selecting disease-relevant biomarkers enhances ASD identification accuracy. Moreover, its logarithmic complexity enables efficient processing of large-scale datasets, supporting real-time clinical applications. By reducing feature dimensionality, GFS-MI also lowers computational cost and improves model efficiency, facilitating deployment in practical settings.

2.3.3. Topological Interaction Graph Neural Network

ASD diagnosis relies on analyzing functional connectivity patterns between neuroanatomical regions, which naturally form graph-structured data through node-edge representations of brain areas and their interactions. Graph convolutional networks (GCNs) directly propagate and aggregate information across this topological structure, systematically incorporating functional dependencies between distinct brain regions. Specifically, the GCN framework performs feature transformation by convolutionally weighting and aggregating nodal features with their topological neighbors, thereby enriching local contextual representations and modeling complex inter-regional relationships. We implement a cascaded architecture with multiple GCN layers, and the input of each layer is the output of the previous layer, for layer-specific updates on whole-brain functional connectivity networks with DMN nodes, the feature propagation is shown in Equation (30):

$$H^{(l+1)} = \sigma(\hat{A}H^{(l)}W^{(l)}). \tag{30}$$

In Equation (30), $H^{(l)}$ is the node feature representation of the l-th layer, $\hat{A}$ is the normalized adjacency matrix (i.e., the union of adjacency matrix A and node degree moment D, $\hat{A} = D^{-1/2}AD^{-1/2}$), $W^{(l)}$ is the learnable weight parameter of layer l, and σ is the ReLU activation function.

Algorithm 1 provides a detailed description of the implementation steps for the BioDiag-Net model. Line 1 projects the whole-brain functional connectivity matrix and the DMN feature matrix into a shared latent space. Lines 2-3 compute the dynamic weighting coefficient α. Line 4 performs weighted fusion of the whole-brain and DMN features. Lines 5-15 use the k-NN method to estimate the entropy and joint entropy of each feature, calculate mutual information, and select highly correlated features. Lines 16-21 transform the selected features into a graph structure representation, compute the similarity matrix as the adjacency matrix, and normalize it. Lines 22-24 implement a multi-layer GCN to update and optimize features layer by layer.

Algorithm 1: The BioDiag-Net Model

Input:

Whole-brain functional connectivity matrix
DMN specific functional connectivity matrix
Y: Target labels

Output:

Optimized feature representation for classification

1: Project A_{whole} and A_{dmn} into a shared latent space
2: $h_{pool} \leftarrow AvgPool(A_{whole} \oplus A_{dmn})$
3: Compute dynamic weighting coefficient α using global average pooling
4: $A_{fused} \leftarrow \alpha * A_{whole} + (1-\alpha) * A_{dmn}$
5: H ← []
6: For each feature F_c in A_{fused} do
7: $H(F_c) \leftarrow$ EstimateEntropy(F_c) // Estimate entropy of feature F_c using k-NN method
8: Append $H(F_c)$ to H
9: **End for**
10: $H(F_c, Y) \leftarrow$ EstimateJointEntropy(F_c, Y)
11: MI ← []
12: For i from 1 to length(H) do
13: $I(F_c, Y) \leftarrow H(F_c) + H(Y) - H(F_c, Y)$.
14: Append $I(F_c, Y)$ to MI

15: **End for**

16: Calculate the similarity matrix between the nodes through the inner product of the feature matrix A_{sim}

17: $A_{sim} \leftarrow$ SymmetricNormalize(A_{sim})

18: $\tilde{A}_{sim} \leftarrow A_{sim}$ + I

19: D $\leftarrow$ DegreeMatrix($\tilde{A}_{sim}$)

20: $\tilde{D} \leftarrow$ InverseSqrt(D)

21: $\hat{A} \leftarrow \tilde{D}^{-1/2}\tilde{A}_{sim}\tilde{D}^{-1/2}$

22: For l from 2 to L do // Iterate over multiple GCN layers

23: Perform graph convolution on the output of the previous layer

24: **End for**

2.4. Novel Loss Function

Finally, the GCN-processed feature representation is fed into a multilayer perceptron (MLP). To optimize feature selection and enhance categorical discriminability, we design a fusion-adaptive loss function that is back-propagated through the network.

2.4.1. Fusion Loss

First, we rank model outputs by feature-label correlation coefficients to identify the most discriminative features. During loss computation, features are dynamically weighted according to their ranked significance, with top-k regions selected for gradient-based optimization. This strategy guides the model to prioritize critical neuroimaging biomarkers while suppressing noisy or irrelevant signals. For each sample, the result after sorting and smoothing by Sigmoid activation function is $H_{sigmoid}$. Based on the probability value of each feature, we define a weighting factor w_f to reflect the contribution of each feature to the loss. It is usually calculated dynamically by the size of the feature value after Sigmoid activation. The weight is calculated by the Equation (31):

$$w_f = H^2_{sigmoid,f} + (1 - H_{sigmoid,f}). \quad (31)$$

Then, the mean weight w_{mean} for each sample is calculated can be expressed as Equation (32):

$$w_{mean} = \frac{1}{F}\sum_{f=1}^{F} w_f . \quad (32)$$

Here, F is the number of features per sample and w_{mean} determines the importance of each sample in training. Top-k loss is calculated by taking the loss of the top k features after sorting. The specific steps are as follows, take the Top-k features from the sorted feature matrix $H_{sigmoid}$, i.e., take out the latter features of the feature matrix (the former features can be understood as the unimportant parts, and the latter k features are the most relevant ones). Calculate the loss of the k features as well as the loss of the rest of the batch. The formula for Top-k loss is shown in Equation (33):

$$L_{top\text{-}k} = -\frac{1}{N}\sum_{i=1}^{N}\log\left[(H_{sigmoid,top\text{-}k} + \zeta)(1 - H_{sigmoid,rest\text{-}k} + \zeta)\right]. \quad (33)$$

In Equation (33), N is the number of samples in the batch, $H_{sigmoid,\ top\text{-}k}$ is the first k features after sorting, and $H_{sigmoid,\ rest\text{-}k}$ is the remaining features.

The contrast loss is to ensure consistency between important features. This is done by calculating the Mean Square Error (MSE) between the Top-k features to guide the model to maintain consistency over the features of interest. The contrast loss is formulated in Equation (34):

$$L_{contrast} = \frac{1}{N}\sum_{i=1}^{N} MSE\left(H_{sigmoid,top\text{-}k}, H_{sigmoid,rest\text{-}k}\right). \quad (34)$$

This step prompts the model to learn the relationship between features by comparing different parts of the features. The final loss is a weighted sum of the Top-k loss and the contrast loss, and also takes into account the weighting factor w_{mean} of the samples, as shown in Equation (35):

$$L_{combined} = \left(L_{top\text{-}k} + L_{contrast}\right) \times w_{mean}. \quad (35)$$

This loss function optimizes the model by weighting it so that important features can get more attention while unimportant features are suppressed.

2.4.2. Cross-Entropy Loss

Cross-entropy measures the difference between the model's predicted probability distribution and the ground truth label distribution. This discrepancy serves as a supervisory signal that guides the model toward optimal learning. The cross-en-

tropy loss function is differentiable, enabling gradient-based optimization methods such as backpropagation through gradient descent [32]. This property facilitates the updating of MLP weights, thereby improving the model's classification performance. In this experiment, our task is a binary classification problem, so the cross-entropy loss is defined in Equation (36):

$$L_{CE} = -\frac{1}{N}\sum_{s=1}^{N}\sum_{c=1}^{C} y_{s,c}\log(\hat{y}_{s,c}) . \quad (36)$$

C is the number of categories (C=2 in this experiment), $y_{s,c}$ denotes the true label of sample s on category c, and $\hat{y}_{s,c}$ represents the predicted probability of the model output.

2.4.3. Final Composite Loss

From this, the total loss of this experiment can be calculated using Equation (37):

$$L_{total} = \lambda_1 L_{CE} + \lambda_2 L_{combined} . \quad (37)$$

Where, λ_1 is the weight of the cross-entropy loss, λ_2 is the weight of the innovation loss, the main role of these weight coefficients is to balance the impact of different loss terms, and finally, the parameters of the MLP are continuously updated and optimized by computing the gradient.

3. Experiments

3.1. Materials

The ABIDE I dataset was employed as described in [8], this publicly shared multicenter MRI repository aggregates data from 17 international sites, with institutional distribution details visualized in Figure 5. The dataset comprises 1,112 participants (539 ASD patients and 573 normal controls), aimed at investigating functional and structural brain abnormalities in ASD.

For each participant, both structural MRI (sMRI) and resting-state fMRI (rs-fMRI) data are included. Additionally, the dataset offers individual behavioral scales to facilitate the investigation of cognitive and behavioral features of ASD.

Figure 5

Proportion of site distribution of data from 17 institutions among ABIDE I.

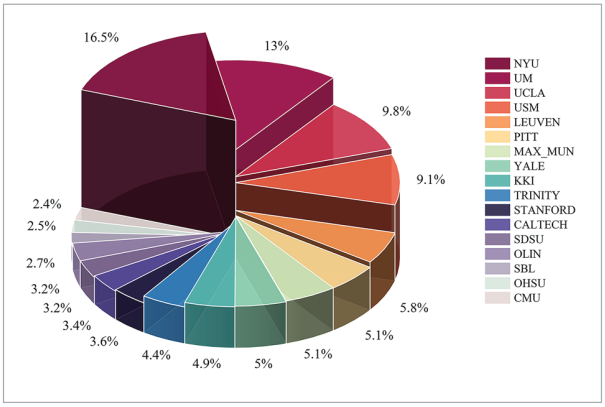

3.1.1. Data Pre-Processing

The Preprocessed Connectomes Project (PCP) provides standardized preprocessed ABIDE I datasets through four computational pipelines [7]. Existing ASD diagnostic studies [18, 25, 27] primarily adopted the Configurable Pipeline for the Analysis of Connectomes (CPAC), which performs essential preprocessing steps including temporal slice correction, head motion compensation, and global intensity normalization. The detailed preprocessing methods and their sequence are illustrated in Figure 6. This diagram presents a total of five specific methods and steps in the preprocessing process. This standardized preprocessing protocol ensures data quality and consistency, thereby providing a robust

Figure 6

The method and detailed steps for PCP to preprocess the ABIDE I dataset using the CPAC pipeline.

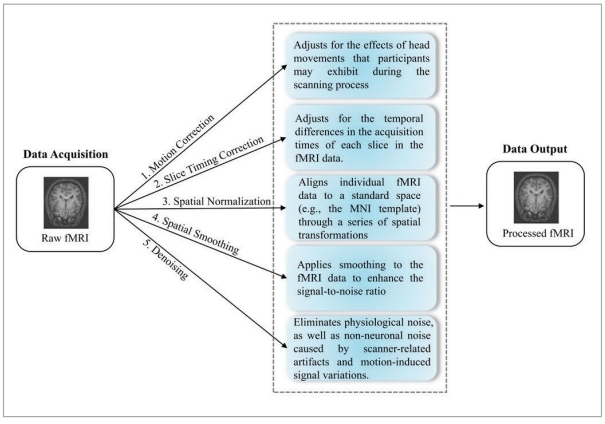

Table 1
The differences in scanning parameters among the four subsets of ABIDE I, where TR denotes repetition time, TE denotes echo time, FOV denotes field of view, Slices denotes number of slices, FLIP Angle denotes flip angle, and Voxel Sise denotes voxel size.

Subset	ASD/NC	TR(sec)	TE(ms)	FOV(mm)	Slices	FLIP Angle	Voxel Size(mm)
STANFORD	19/20	2	30	200	29	80	3.13 × 3.13 × 4.50
UCLA	54/44	3	28	192	34	90	3.00 × 3.00 × 4.00
NYU	75/100	2	15	240	33	90	3.00 × 3.00 × 4.00
UM	66/74	2	30	220	40	90	3.44 × 3.44 × 3.00

foundation for subsequent analyses. Importantly, the CPAC demonstrates unique technical advantages over conventional neuroimaging pipelines (e.g., FSL, SPM, AFNI) through its distributed computing architecture that enables large-scale multi-site data harmonization.

This computational framework ensures cross-institutional comparability by minimizing scanner and protocol-related variances [2]. Notably, the integrated functional connectivity analysis module in CPAC enables direct extraction of connectivity matrices from preprocessed data, a critical capability that supported subsequent analytical phases in this investigation.

Following [8], we performed rigorous quality control, excluding subjects with excessive motion artifacts, scanner malfunctions, incomplete imaging sequences, or insufficient scan duration. This protocol yielded 1,035 high-quality datasets with validated diagnostic accuracy. For multisite validation, we stratified and sampled from Stanford, UCLA, NYU, and the University of Michigan, with the acquisition parameters presented in Table 1. This design evaluates both model generalizability across heterogeneous scanners and diagnostic consistency in clinical environments.

3.1.2. Experimental Setup

To evaluate model performance, we employed stratified 5-fold epoch by partitioning the 1,035 samples into five demographically balanced cohorts. Each fold designates one cohort as the validation set, with the remaining four used for model training and hyperparameter optimization via backpropagation. This protocol enables unbiased performance estimation while ensuring comprehensive assessment of generalizability across multi-site ASD data through five complete iterations. The training regimen comprised 300 epochs per fold using mini-batch SGD (batch size=16) with the Adam optimizer (initial learning rate=1e-4), balancing convergence stability and update precision. Experimental reproducibility was guaranteed through fixed random seed initialization (seed=42).

The computational framework utilized PyTorch 2.1.2 with scientific computing libraries, accelerated by an NVIDIA GeForce RTX 4090 GPU (8,176 CUDA cores, 24GB GDDR6X VRAM) using mixed-precision training.

3.2. Diagnostic Results

We conducted experiments on the full sample (N = 1035) and the four site-stratified subsets (Stanford, UCLA, NYU, Michigan). The classification results are shown in Table 2, which details the performance metrics such as Accuracy (ACC), Sensitivity (SEN), Specificity (SPE), Area Under the ROC Curve (AUC), F1-Score, and Matthews Correlation Coefficient (MCC), higher metric values indicate superior diagnostic capability. The first six metrics are commonly used to evaluate model performance. Specifically, MCC is a measure of classification model quality that takes into account true positives, false positives, true negatives, and false negatives. In autism diagnosis, particularly in cases of data imbalance, MCC provides a more reliable evaluation result. The calculation formula is shown in Equation (38):

$$\mathrm{MCC} = \frac{TP \times TN - FP \times FN}{\sqrt{(TP + FP)(TP + FN)(TN + FP)(TN + FN)}}. \quad (38)$$

Here, TP is the number of true positives, TN is the number of true negatives, FP is the number of false positives, and FN is the number of false negatives.

The BioDiag-Net framework achieved 83.48% overall accuracy with site-specific performance reaching 100% (Stanford), 100% (UCLA), 98.15% (NYU), and 99.23% (Michigan), demonstrating robust generalizability across multi-center data. Figure 7 shows the distribution of original samples (a) and the distribution of sample characteristics (b) after classification by our proposed method. It can be observed that the distribution of original samples before classification was disorderly, whereas the distribution of samples after classification by our proposed method was significantly regularized.

Figure 7

(a) Original sample distribution and (b) sample feature distribution after MLP classification.

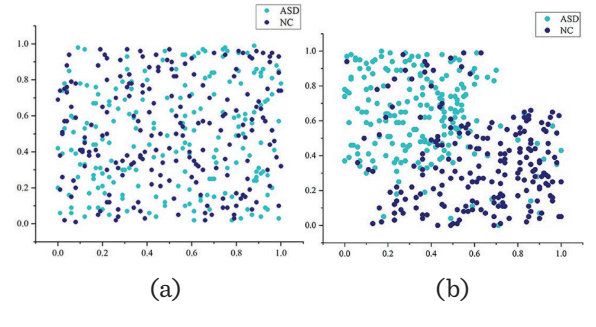

As shown in Figure 8, the training loss curve on the CC200 atlas exhibits a consistent downward trend, indicating stable convergence during optimization.

Quantitative comparisons demonstrated statistically significant superiority in site-specific cohorts versus the aggregated dataset across all metrics.

This performance divergence primarily originates from cross-site heterogeneity in imaging protocols,

Figure 8

Training loss evolution curves for each of the five folds in the cross-validation.

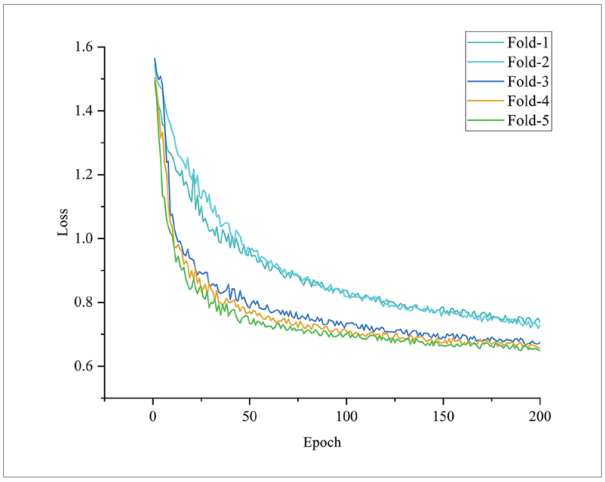

scanner manufacturers, and demographic distributions. Conversely, intra-site datasets exhibited enhanced feature consistency and mitigated class imbalance. Notably, Stanford and UCLA cohorts showed optimal performance attributable to optimized signal-to-noise ratios, balanced case-control distributions, and standardized acquisition protocols.

3.3. Comparative Diagnostic Methods

To comprehensively evaluate the performance of the model from multiple perspectives, we classify the collected existing methods into two main categories: Non-Graph-based and Graph-based. Non-Graph-based methods utilize non-graph structures with interpretable decision processes but neglecting brain network topology, resulting in suboptimal performance. The Graph-based category encom-

Table 2

The classification performance of the BioDiag-Net, assessed in terms of accuracy, sensitivity, specificity, AUC, precision, F1-Score and MCC was evaluated across the ABIDE I dataset and its subsets.

Dataset	Subjects	SEN (%)	SPE (%)	ACC (%)	AUC (%)	PRE (%)	F1-Score (%)	MCC
ABIDE I	1,035	85.13	80.06	83.48	86.78	84.56	84.89	0.75
STANFORD	39	100.00	100.00	100.00	100.00	100.00	100.00	1.00
UCLA	98	100.00	100.00	100.00	100.00	100.00	100.00	1.00
NYU	175	96.67	94.00	98.15	97.80	95.25	95.95	0.93
UM	140	98.48	96.49	99.23	99.10	97.85	98.16	0.96

passes methods capable of processing irregular graph-structured data, offering a unique advantage for addressing functional brain connectivity disorders like autism, yet exhibiting limited diagnostic-specific optimization. The experimental results of the comparison with previous methods are shown in Table 3. Although existing methods have made progress in diagnosing ASD, significant limitations remain in model design, data utilization, and clinical applicability. The following is a summary and analysis of the limitations of existing methods.

Eslami et al. [9]: This method uses joint training of autoencoders and perceptrons with linear interpolation for data augmentation but lacks explicit brain region interaction modeling, potentially missing ASD-related network abnormalities.

Liu et al. [17]: The Extra-Trees algorithm combined with attention-based feature selection and SVM is used for ASD classification. However, the linear separability assumption by SVM contradicts fMRI's non-linear nature, reducing effectiveness.

Niu et al. [19]: Multimodal fusion of fMRI and demographic features using a multi-channel deep attention network (DANN). However, this approach may mask imaging features in small samples, reducing biological interpretability.

Liu et al. [16]: A weighted DNN ensemble based on multiple atlases (AAL+CC200+EZ) for ASD diagnosis. However, integrating multiple atlases without theoretical support can lead to high-dimensional feature spaces, causing the curse of dimensionality.

Kong et al. [15]: A DNN classifier based on structural connectivity for ASD/TC classification. Overfitting is a concern due to the use of 3000 high F-score features in a small sample size.

Wen et al. [27]: A multitask graph convolutional network guided by prior brain structure for ASD diagnosis. However, static graph construction fails to account for dynamic functional connectivity fluctuations.

Jiang et al. [12]: A hierarchical graph convolutional network framework learns graph feature embeddings while considering network topology and subject associations. However, this approach may amplify site biases and reduce interpretability.

Wang et al. [25]: A graph encoder extracts time-correlated features with long-range dependencies using residual techniques. However, relying solely on Pearson correlation ignores non-linear functional connectivity dynamics.

Ma et al. [18]: Multiple atlases are fused based on spatial overlap, and a GCN is used for final classification. High-dimensional fusion requires strict regu-

Table 3

The results of the comparison with previous methods, are measured in terms of sensitivity, specificity, and accuracy of classification.

Category	Study	Subjects	Atlas	SEN (%)	SPE (%)	ACC (%)
	Eslami et al. [9]	1,035	CC200	68.30	72.20	70.30
	Liu et al. [17]	1,054	CC200	68.60	75.40	72.20
Non-Graph-based	Niu et al. [19]	809	AAL+HO+CC200	74.50	71.70	73.20
	Liu et al. [16]	1,035	CC200+AAL+EZ	82.90	69.70	75.20
	Kong et al. [15]	182	Destrieux	84.37	95.88	90.39
	Wen et al. [27]	871	AAL	69.81	64.45	69.38
	Jiang et al. [12]	868	AAL	71.40	74.60	73.10
Graph-based	Wang et al. [25]	1,035	CC200	75.20	73.40	74.40
	Ma et al. [18]	732	CC200+AAL+EZ+HO+TT	64.20	81.30	75.70
	Gu et al. [11]	871	Harvard-Oxford	95.30	91.32	93.40
	Ours	1,035	CC200	85.13	80.06	83.48

larization, and spatial overlap assumptions may not apply to children's ASD brains.

Gu et al. [11]: This method proposes a heterogeneous graph neural network (FC-HGNN) based on brain functional connectivity, an end-to-end model with two stages. However, the complex architecture may overfit the Harvard-Oxford atlas used in the study.

These existing methods collectively face overfitting risks, including small sample sizes, atlas-specific biases, and static connectivity assumptions. These risks may lead to good performance on training data but poor performance on new, unseen data, thereby limiting the model's generalizability and clinical applicability. When evaluated on the multicenter cohort (N=1,035), our model achieved an overall accuracy of 83.48%. To rigorously validate methodological superiority, we conducted comparative analyses against three state-of-the-art approaches [9, 16, 25] that utilized the identical cohort. As demonstrated in Figure 9, BioDiag-Net statistically significantly outperformed all comparative methods across comprehensive evaluation metrics.

Figure 9

Comparison of the performance of the study results for the experiments also using 1035 samples.

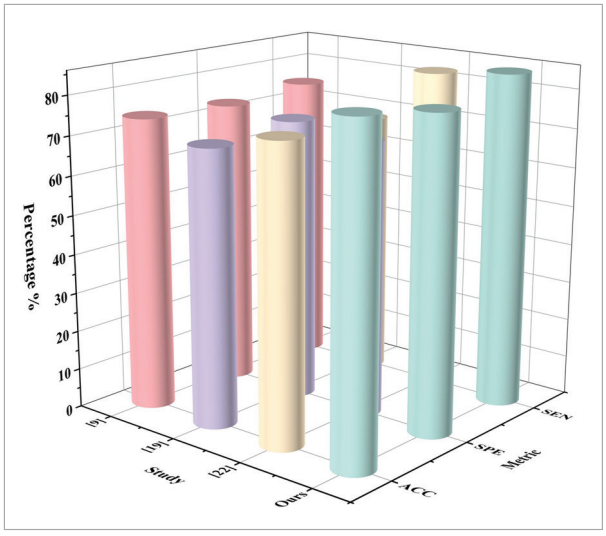

It is noteworthy that Ma et al. [18] achieved the second-highest accuracy rate after our BioDiag-Net when using the same number of samples. This can be attributed to their incorporation of demographic phenotypic information, a factor worthy of consideration in future research. Notably, our model maintains robust performance on ABIDE I subsets such as NYU and UCLA despite incomplete multi-site data usage, highlighting its cross-site generalizability through optimized architecture. Moreover, the comparison results highlight that the quality of different datasets can potentially influence classification outcomes. It can be inferred that reasonable data selection and preprocessing across subsets are crucial for enhancing model performance in autism diagnosis tasks.

To comprehensively evaluate the computational efficiency and resource requirements of existing models, we conducted a systematic quantitative analysis on four studies [9, 11, 19, 25] from Table 3 that provide complete experimental protocols, including open-source code and detailed hardware/software configurations. These models demonstrate strong performance in ASD diagnosis but exhibit notable differences in terms of computational cost and runtime efficiency. For models lacking environmental specifications, we aligned their implementation settings with those of BioDiag-Net to ensure fair comparison. In Table 4, we summarize key performance metrics such as cross-validation setup, training epochs, hardware configuration, GPU memory usage, inference latency, and floating-point operations (FLOPs). Experimental results show that BioDiag-Net adopts a 5-fold cross-validation strategy, which better balances reliability and efficiency. Mixed-precision training is employed to reduce VRAM consumption. High CUDA core utilization further lowers inference latency, while the GFS-MI module prunes redundant connections and reduces computational complexity, as reflected by lower FLOPs.

3.4. Analysis of Methodological Novelty and Effectiveness

3.4.1. Motivation of the Proposed Method

SPI: Conventional GNN-based models treat brain regions as unordered nodes, neglecting their 3D anatomical positions and hierarchical relationships. However, ASD-related connectivity abnormalities often exhibit spatial locality. To address this, SPI introduces multi-frequency positional encoding to model node distances at multiple scales, enhancing spatial awareness for improved detection of ASD-specific patterns.

Table 4
Comparative evaluation table of computational efficiency and performance across ASD diagnostic models.

Study	Cross-validation	Epochs	Hardware	VRAM (GB)	Latency (ms)	FLOPs (G)
Wang et al. [25]	5-CV	500	RTX 4090 GPU	13.8	17.9 ± 2.0	31.8
Eslami et al. [9]	10-CV	300	Tesla K-40c GPU	14.6	15.2 ± 1.8	30.7
Niu et al. [19]	5-CV	300	TITAN Xp GPU	10.2	18.6 ± 2.3	27.4
Gu et al. [11]	10-CV	400	RTX 4090 GPU	14.7	22.4 ± 3.1	35.3
Ours	5-CV	300	RTX 4090 GPU	11.3	14.5 ± 0.8	24.1

CCIF: CCIF is motivated by the observation that traditional methods handle multi-scale brain networks (e.g., whole-brain and DMN) using static feature fusion strategies like fixed-weight averaging or simple concatenation. These approaches cannot dynamically adjust feature importance based on individual samples, potentially masking noise or redundant features while overlooking key pathological information. CCIF addresses this with a context-aware attention mechanism that dynamically weights and integrates multi-scale features, prioritizing relevant connectivity patterns in each individual.

GFS-MI: High-dimensional functional connectivity features often contain redundant or irrelevant connections. Traditional selection methods (e.g., L1, thresholding) ignore higher-order interactions and network coherence, potentially missing diagnostically meaningful biomarkers. GFS-MI overcomes this by selecting features based on mutual information maximization with ASD labels, reducing redundancy while preserving interpretability and mitigating overfitting.

3.4.2. Ablation Study and Justification Analysis

To evaluate the contribution of each component in BioDiag-Net, we conducted a comprehensive ablation study using the CC200 atlas. The evaluation metrics include accuracy, sensitivity, specificity, AUC, precision, F1-score, and MCC, as summarized in Table 5.

Removing the SPI module significantly impairs model performance by limiting its ability to capture spatial relationships between brain regions. As node order and location carry biological significance in graph-structured data, the absence of positional embedding leads to superficial modeling of functional connectivity. This results in a drop in diagnostic accuracy to 80.45%, compared to the full model, the result validates the importance of incorporating SPI, which aids the model in better understanding biologically meaningful spatial connectivity patterns.

The CCIF module is essential for integrating features from whole brain functional connectivity and DMN. Its removal leads to a 7.59% drop in accuracy, along with decreases of 13.18% in sensitivity and 8.25% in specificity. This performance decline stems from the loss of complementary biological information especially inter ROI correlations highlighting CCIF's role in dynamically fusing multi scale features and enabling more comprehensive capture of autism related neural patterns.

Finally, disabling the GFS-MI module reduces the model's ability to filter relevant features from

Figure 10
Variation curve of feature number and accuracy after feature selection by GFS-MI module.

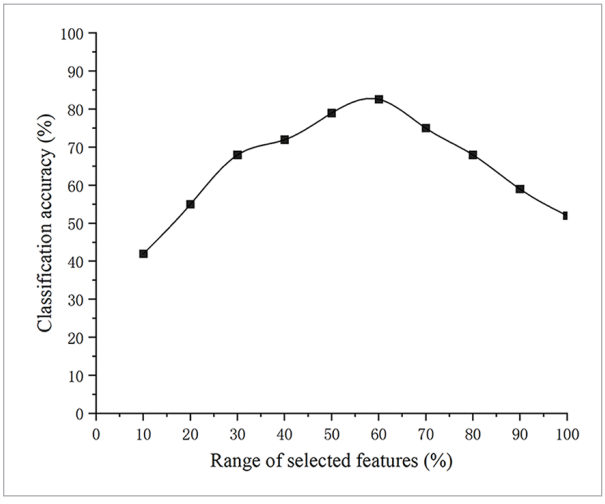

high-dimensional inputs. Diagnostic accuracy drops sharply to 79.33% without it. As shown in Figure 10, classification accuracy improves with increasing feature selection up to approximately 60%, after which further expansion leads to performance degradation due to overfitting or redundancy. These findings demonstrate that GFS-MI enhances model efficiency by retaining autism-relevant features while eliminating noise and redundancy.

3.4.3. Comparative Analysis of Method Characteristics

To compare the key technical design differences between the proposed BioDiag-Net and existing ASD diagnostic methods, we constructed a feature comparison table. In this table, "Full Support" indicates that the compared model fully employs the technique, "No Support" indicates that the compared model does not employ the technique, and "Partial Support" indicates that only some functions of the listed features are met. We conducted a comprehensive comparison across multiple dimensions, including model structure type, interpretability, end-to-end design, DMN feature integration, neural spatial encoding, whether the feature fusion mechanism is dynamic, consideration of higher-order feature interactions in experiments, and feature selection combined with graph structure. The specific results are presented in Table 6.

Table 5

The ablation results of different components in BioDiag-Net. SPI denotes Spatial Prior Injection, CCIF denotes Cross-Channel Interaction Fusion, and GFS-MI denotes Node Filtering Method based on Graph Feature Selection with Mutual Information Maximization.

SPI	CCIF	GFS-MI	SEN (%)	SPE (%)	ACC (%)	AUC (%)	PRE(%)	F1-Score (%)	MCC
✗	✓	✓	78.69	75.31	80.45	81.23	80.12	79.56	0.68
✓	✗	✓	72.05	71.81	75.02	75.43	73.21	72.65	0.62
✓	✓	✗	77.28	74.80	79.33	78.90	76.54	77.02	0.66
✓	✓	✓	85.23	80.06	83.48	86.78	84.56	84.89	0.75
✗	✗	✗	68.97	66.53	70.25	71.05	69.48	68.93	0.53

Table 6

Characteristic Comparison Table. Here, HPG denotes Heterogeneous Population Graph, BAT denotes Bat Algorithm, PSO denotes Particle Swarm Optimization, and LSTM denotes Long Short-Term Memory.

Study	Ma et al. [18]	Gu et al. [11]	Khan et al. [14]	Pan et al. [21]	Ours
Model Architecture Type	Multi-atlas Fusion+GCN	GCN+HPG	BAT+PSO +LSTM	GCN+Multi-channel Fusion	GCN+MLP
Interpretability	Full Support	Full Support	Full Support	No Support	Full Support
End-to-End Training	Full Support	Full Support	Full Support	Full Support	Full Support
DMN Feature Integration	No Support	No Support	No Support	No Support	Full Support
Neural Spatial Encoding	No Support	No Support	No Support	No Support	Full Support
Dynamic Feature Fusion	Partial Support	No Support	Full Support	Full Support	Full Support
Higher-Order Feature Interactions	Full Support	Full Support	Partial Support	Full Support	Full Support
Graph-Based Feature Selection	Full Support	Partial Support	No Support	Full Support	Full Support

3.5. Visualization Analysis of ROI Distributions

3.5.1. Circular Heatmap of ASD-Related ROIs

We randomly selected one autism patient (a) and one normal control (b) from the University of Pittsburgh Medical Center. Based on the CC200 atlas, we extracted the BOLD time series from 200 brain regions (ROIs), which reflect the changes in blood oxygenation levels over time in each region. By calculating the Pearson correlation coefficients between each pair of ROIs, we constructed a 200×200 functional connectivity matrix $C \in R^{200\times200}$, where C_{ij} represents the functional connectivity strength between the i-th and j-th brain regions. Using Origin 2024, we generated a circular heatmap. The labels surrounding the circular heatmap correspond to the ROIs in the CC200 atlas that are significantly abnormal in the autistic patient. The brain region serial numbers and tag files are published by PCP. As shown in Figure 11, brain regions surrounding the autism sample are labeled and correspond closely to those associated with the DMN, aligning with data points in the central dendrogram. The dendrogram within the circular heatmap corresponding to the autism patient demonstrated significant height variations and an irregular edge contour. In contrast, the dendrogram of the neurotypical control exhibited a relatively uniform height and a smooth, continuous arc along its edge.

Figure 11

(a) Visualization of a circular heat map based on Pearson correlation calculations for ASD samples and (b) NC samples

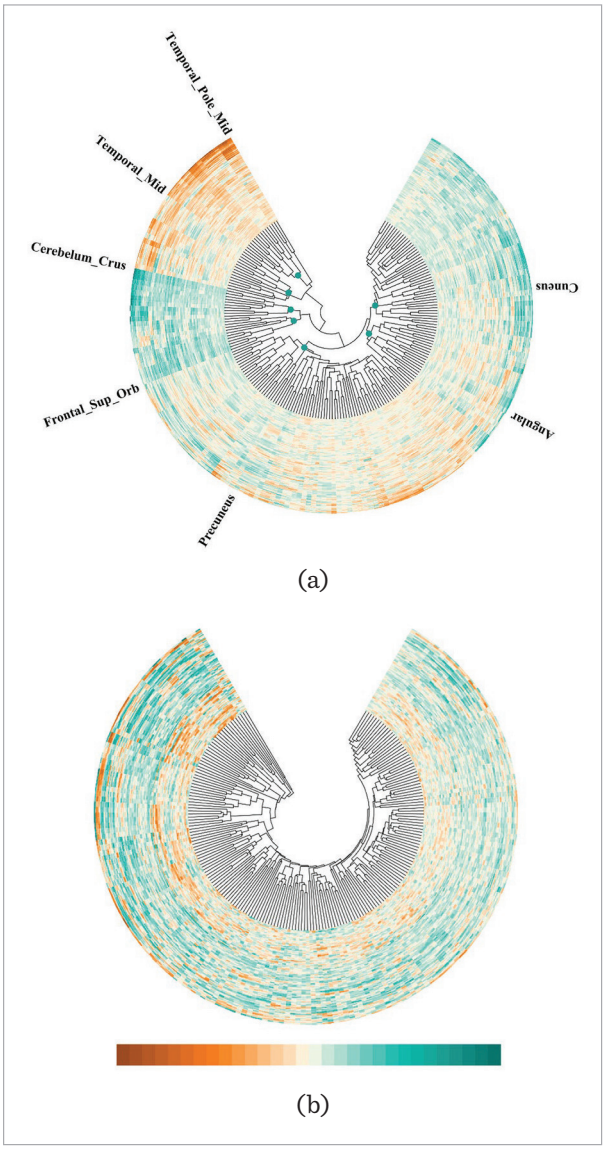

Labeled ROIs indicate distinct correlation patterns in autism, diverging from typical controls, suggesting potential biomarkers. These findings provide novel insights into the unique neural connectivity profiles in autism spectrum disorder.

3.5.2. Connectivity Graph of DMN-Related Nodes and Edges

As described in Section 3.5.1, we identified significantly abnormal brain regions within the DMN by calculating the Pearson correlation coefficients between brain regions based on the CC200 atlas. The data annotations in Figure 12 are sourced similarly to the previous section. By referencing the serial numbers of significant brain regions, the corresponding ROI labels can be located in the CC200 atlas, and the figure was generated using BrainNet Viewer [28], sequentially displays the three standard anatomical views of the brain—sagittal (a), axial (b), and coronal (c). In this visualization, ROIs that exhibit either a direct or indirect relationship with DMN are represented by larger nodes compared to other nodes and are labeled with their respective names.

Additionally, the visualization reveals that key nodes of DMN, form a distinct cluster characterized by prominent features. Prior studies [6, 24] have identified notable anomalies in the functional connectivity within DMN among individuals diagnosed

with autism. These investigations demonstrate that the overall connectivity strength between various DMN regions is diminished in autistic individuals relative to neurotypical controls. This attenuation of connectivity is posited to contribute to challenges in social cognition, potentially impairing the ability of individuals to accurately discern others' emotions, behaviors, and intentions.

For example, it has been highlighted by [3] that while the clinical symptoms of autism might involve specific brain regions, the neurobiological basis of autism is more accurately described by the complex interactions and interconnections among multiple, distributed brain regions rather than by a single focal area. In this light, the brain characteristics of autism are perceived as segmented and multifaceted. This organized network structure greatly enhances the efficacy of using DMN-based biomarkers for the diagnosis of ASD.

3.5.3. Annotated Top 10 Critical Brain Regions

Section 2 elaborates on the implementation of a node screening method that employs graph-based feature selection through mutual information maximization. This method quantifies the mutual information between each node feature and the target label, preserving features with substantial contributions to label prediction and omitting those with minimal correlation.

Figure 13 illustrates that a template from the CC200 atlas was used. Ten distinct colors were applied to delineate the top 10 ROIs. Similarly, the data annotations in the figure are derived from the ROI labels in the CC200 atlas provided by PCP. Consistent with previous studies [4, 30], our results further confirm the close association of these brain regions with ASD-related neurodevelopmental abnormalities. This not only validates the effectiveness of our identification method but also offers a new perspective for understanding the neurobiological basis of ASD.

Next, the regions were mapped across various brain dimensions. This included the lateral and medial aspects of each hemisphere and the dorsal, ventral, anterior, and posterior segments. Notably, these ROIs correlate with the severity of repetitive and stereotyped behaviors, as well as social interaction deficits in autistic patients. Figure 14 ranks the top 10 autism-associated brain regions from our feature

Figure 12

Three labeled views of DMN-related ROI nodes, representing (a) Sagittal, (b) Axial, and (c) Coronal.

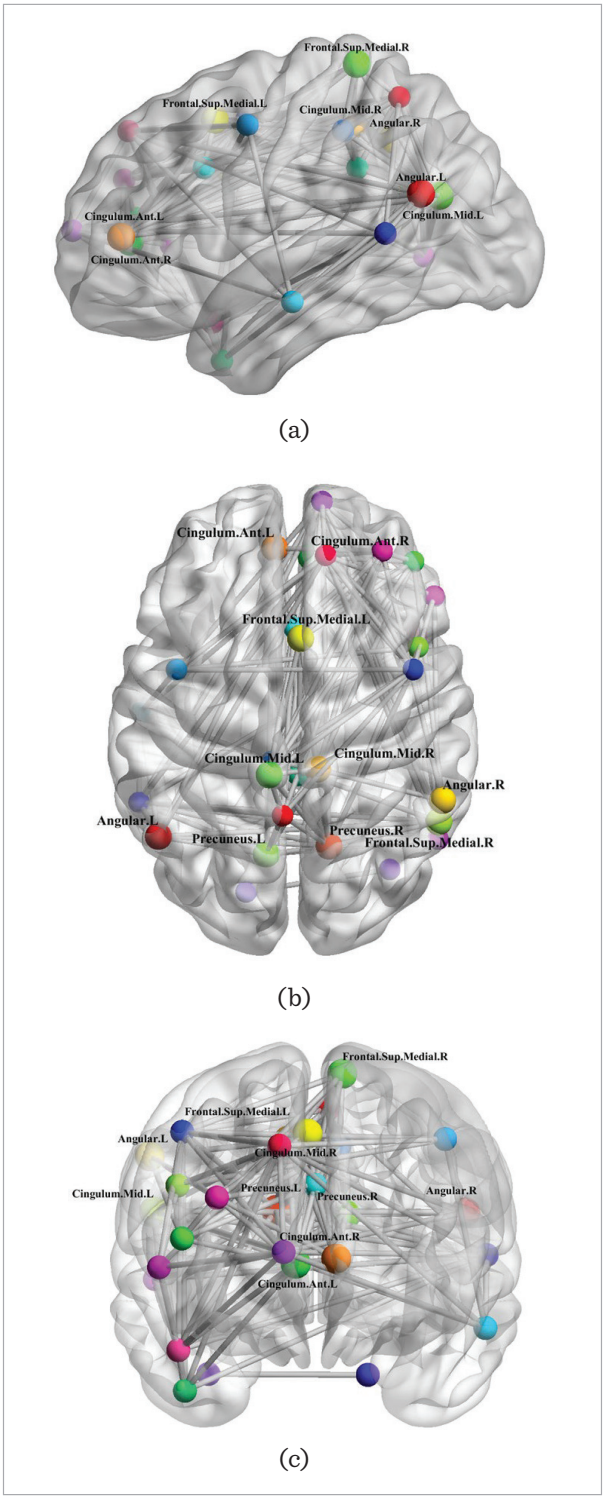

Figure 13
Annotation of the top 10 detected ROIs showing strong coupling with ASD neurodevelopmental abnormalities based on the CC200 Atlas template base.

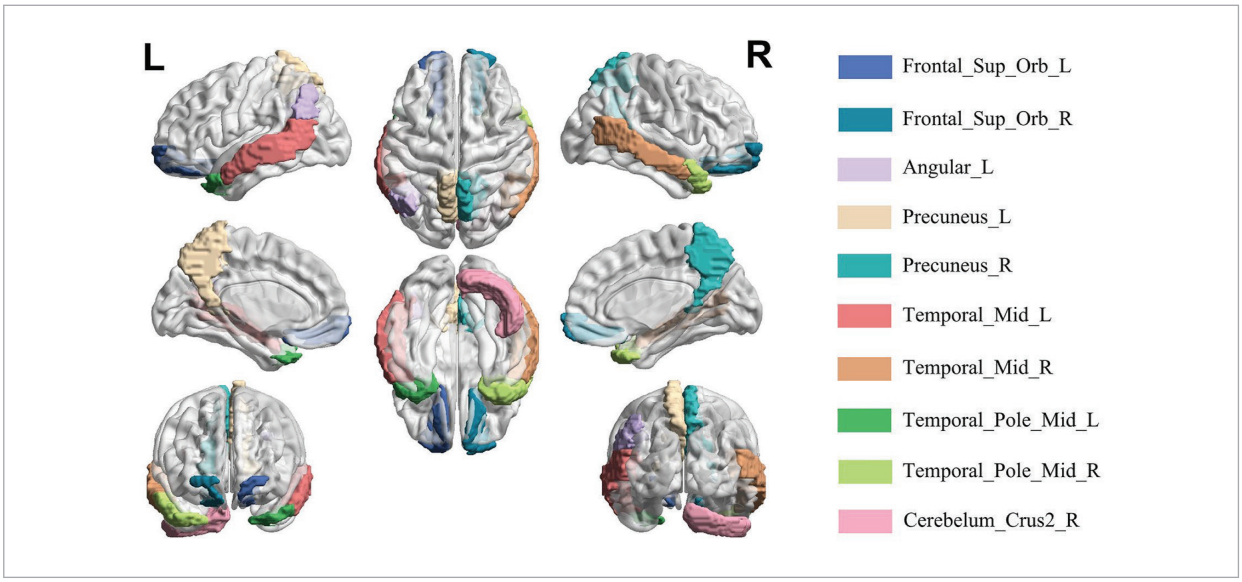

Figure 14
Importance ranking of the top ten most relevant brain.

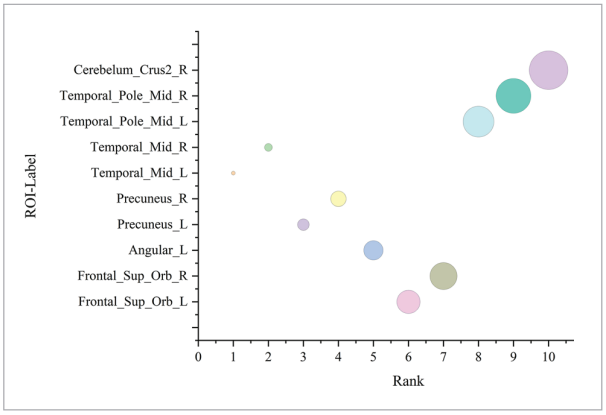

selection pipeline. Their spatial distribution validates their pathological relevance in ASD neurobiology and underscores the importance of integrating DMN-derived features and biological priors into neuro-imaging-based diagnostic frameworks.

4. Conclusion

To address the critical limitations of traditional behavioral scale-based ASD diagnosis, including subjective assessment bias, insufficient early detection capacity, and global disparities in clinical resources, we propose BioDiag-Net, a neuroimaging-driven diagnostic framework that integrates three synergistic innovations. The architecture first incorporates a spatial prior injection module that explicitly encodes neuroanatomical coordinates of brain regions, overcoming conventional models' inability to model spatial dependencies. A cross-domain alignment module then establishes biological prior-guided interactions between whole-brain functional connectivity and DMN dynamics, enabling focused analysis of ASD-specific neural circuitry. Complementing these components, an information-theoretic node selection mechanism eliminates redundant features through mutual information maximization, retaining clinically interpretable biomarkers. Validated on the ABIDE I dataset (1,035 multisite rs-fMRI scans), BioDiag-Net achieves state-of-the-art classification accuracy (83.48%) across heterogeneous patient cohorts, demonstrating superior generalizability. This framework pioneers a paradigm shift toward quantitative and standardized ASD diagnostics by enabling (1) early neural signature detection during presymptomatic stages through multidimensional pattern analysis, and (2) intelligent decision-support for tiered healthcare systems via explainable biomarker

visualization. By bridging deep learning with neurobiological insights, BioDiag-Net lays the foundation for scalable, interpretable neurodevelopmental disorder diagnostics.

5. Limitations and Future Prospects

Although BioDiag-Net has demonstrated remarkable performance in the diagnosis of autism, it still has certain limitations. First, reliance on standard brain atlases may not fully account for the individual anatomical variations in autistic patients, especially in the developing brains of children. Future research could consider incorporating individualized brain region segmentation using structural MRI to enhance the adaptability and accuracy of the model. Second, the current interaction between the whole brain and the DMN has not explicitly modeled instantaneous functional states. Introducing temporal graph networks could enhance the model's sensitivity in the temporal dimension, thereby more accurately capturing dynamic functional changes. Finally, autism is a multiscale neuro-developmental disorder, and the current diagnostic task primarily relies on fMRI, lacking validation with multimodal data. Integrating structural imaging or genomic data to build a structure-function joint model could not only improve diagnostic performance but also potentially reveal multiscale biomarkers, providing a more comprehensive basis for the early diagnosis and intervention of autism.

Gao et al. [10] proposed a density-based time series clustering model (DCMD) that effectively reduces the dimensionality of time series data through a multidimensional representation fusion module and a K-nearest neighbor weighted clustering module. This method excels in handling high-dimensional data and complex distributions, providing valuable insights for diagnosing ASD using rs-fMRI data. Yang et al. [29] also introduced a point cloud upsampling network (DGCMSA-PU). The network dynamically constructs graph structures via edge convolution, extracts features using multi-head attention mechanisms, and reconstructs 3D coordinates through an up-down-up structure. Experimental results demonstrate that DGCMSA-PU exhibits robustness against noise and varying numbers of inputs. Its innovations in dynamic graph structure modeling and multi-head attention mechanisms offer important reference for dealing with biomedical data related to network structures. These methods hold promise for more effectively extracting deeper dynamic features from individuals with ASD, thereby enhancing diagnostic accuracy and reliability.

Conflict of Interest

The authors declare that they have no conflicts of interest related to this study. The research presented here has been conducted with full impartiality and transparency, free from external pressures, affiliations, or influences that could compromise its integrity. The authors are solely responsible for the content and conclusions drawn in this work.

Data Availability Statement

The datasets and materials supporting the findings of this study are available from the corresponding author upon reasonable request, subject to privacy and ethical standards. Researchers seeking access should provide a clear rationale for their request. The corresponding author will facilitate access whenever possible to support further inquiry and knowledge advancement.

References

1. Almuqhim, F., Saeed, F. ASD-SAENet: A Sparse Autoencoder, and Deep-Neural Network Model for Detecting Autism Spectrum Disorder (ASD) Using fMRI Data. Frontiers in Computational Neuroscience, 2021, 15, 654315. https://doi.org/10.3389/fncom.2021. 654315
2. Cameron, C., Sharad, S., Brian, C., Ranjeet, K., Michael, M. Towards Automated Analysis of Connectomes: The Configurable Pipeline for the Analysis of Connectomes (C-PAC). Frontiers in Neuroinformatics, 2013, 7. https://doi.org/10.3389/conf.fninf.2013.09.00042.
3. Chen, C.P., Keown, C.L., Jahedi, A., Nair, A., Pflieger, M.E., Bailey, B.A., Müller, R.-A. Diagnostic Classification of Intrinsic Functional Connectivity highlights somatosensory, default mode, and visual Regions

in Autism. NeuroImage: Clinical, 2015, 8, 238-245. https://doi.org/10.1016/j.nicl.2015.04.002

4. Cheng, W., Rolls, E.T., Gu, H., Zhang, J., Feng, J. Autism: Reduced Connectivity Between Cortical Areas Involved in Face Expression, Theory of Mind, and the Sense of Self. Brain, 2015, 138, 1382-1393. https:// doi.org/10.1093/brain/awv051
5. Chen, H., Duan, X., Liu, F., Lu, F., Ma, X., Zhang, Y., Uddin, L.Q., Chen, H. Multivariate Classification of Autism Spectrum Disorder Using Frequency-Specific Resting-State Functional Connectivity-A Multi-Center Study. Progress in Neuro-Psychopharmacology and Biological Psychiatry, 2016, 64, 1-9. https:// doi. org/10.1016/j.pnpbp.2015.06.014
6. Chen, L., Chen, Y., Zheng, H., Zhang, B., Wang, F., Fang, J., Li, Y., Chen, Q., Zhang, S. Changes in the Topological Organization of the Default Mode Network in Autism Spectrum Disorder. Brain Imaging Behavior, 2021, 15, 105-81067. https://doi.org/10.1007/s11682-020-00312-8
7. Craddock, C., Benhajali, Y., Chu, C., Chouinard, F., Bellec, P. The Neuro Bureau Preprocessing Initiative: Open Sharing of Preprocessed Neuroimaging Data and Derivatives. Frontiers in Neuroinformatics, 2013, 7. https:// doi.org/10.3389/conf.fninf.2013.09.00041
8. Di Martino, A., Yan, C.-G., Li, Q., Denio, E., Castellanos, F.X., Alaerts, K., Anderson, J.S., Assaf, M., Bookheimer, S.Y., Dapretto, M., Deen, B., Delmonte, S., Dinstein, I., Ertl-Wagner, B., Fair, D.A., Gallagher, L., Kennedy, D.P., Keown, C.L., Keysers, C., Lainhart, J.E., Lord, C., Luna, B., Menon, V., Minshew, N.J., Monk, C.S., Mueller, S., Müller, R.-A., Nebel, M.B., Nigg, J.T., O'Hearn, K., Pelphrey, K.A., Peltier, S.J., Rudie, J.D., Sunaert, S., Thioux, M., Tyszka, J.M., Uddin, L.Q., Verhoeven, J.S., Wenderoth, N., Wiggins, J.L., Mostofsky, S.H., Milham, M.P. The Autism Brain Imaging Data Exchange: Towards a Large-Scale Evaluation of the Intrinsic Brain Architecture in Autism. Molecular Psychiatry, 2014, 19, 659-667. https://doi.org/ 10.1038/mp.2013.78
9. Eslami, T., Mirjalili, V., Fong, A., Laird, A.R., Saeed, F. ASD-DiagNet: A Hybrid Learning Approach for Detection of Autism Spectrum Disorder Using fMRI Data. Frontiers in Neuroinformatics, 2019, 13, 70. https:// doi.org/10. 3389/fninf.2019.00070
10. Gao, J., Guo, Y., Li, C., Wang, H., Zhao, X., Li, T., Li, X. Multi-Dimensional Temporal Feature Fusion and Density Perception for Time Series Clustering. Information Technology and Control, 2025, 54, 16-31. https://doi.org/10.5755/j01.itc.54.1.38771
11. Gu, Y., Peng, S., Li, Y., Gao, L., Dong, Y. FC-HGNN: A Heterogeneous Graph Neural Network Based on Brain Functional Connectivity for Mental Disorder Identification. Information Fusion, 2025, 113, 102619. https:// doi.org/10.1016/j.inffus.2024.102619
12. Jiang, H., Cao, P., Xu, M., Yang, J., Zaiane, O. Hi-GCN: A Hierarchical Graph Convolution Network for Graph Embedding Learning of Brain Network and Brain Disorders Prediction. Computers in Biology and Medicine, 2020, 127, 104096. https://doi.org/10.1016/ j.compbiomed.2020.104096
13. Kazeminejad, A., Sotero, R.C. Topological Properties of Resting-State fMRI Functional Networks Improve Machine Learning-Based Autism Classification. Frontiers in Neuroscience, 2019, 12, 1018. https://doi. org/10.3389/fnins. 2018.01018
14. Khan, K., Katarya, R. AFF-BPL: An Adaptive Feature Fusion Technique for the Diagnosis of Autism Spectrum Disorder Using Bat-PSO-LSTM Based Framework. Journal of Computational Science, 2024, 83, 102447. https://doi.org/10.1016/j.jocs.2024.102447
15. Kong, Y., Gao, J., Xu, Y., Pan, Y., Wang, J., Liu, J. Classification of Autism Spectrum Disorder by Combining Brain Connectivity and Deep Neural Network Classifier. Neurocomputing, 2019, 324, 63-68. https://doi. org/10.1016/j.neucom.2018.04.080
16. Liu, X., Hasan, M.R., Gedeon, T., Hossain, M.Z. MADE-for-ASD: A Multi-Atlas Deep Ensemble Network for Diagnosing Autism Spectrum Disorder. Computers in Biology and Medicine, 2024, 182, 109083. https://doi. org/10.1016/j.compbiomed.2024.109083
17. Liu, Y., Xu, L., Li, J., Yu, J., Yu, X. Attentional Connectivity-Based Prediction of Autism Using Heterogeneous rs-fMRI Data from CC200 Atlas. Experimental Neurobiology, 2020, 29, 27-37. https:// doi.org/10.5607/ en.2020.29.1.27
18. Ma, Y., Mu, X., Zhang, T., Zhao, Y. MAFT-SO: A Novel Multi-Atlas Fusion Template Based on Spatial Overlap for ASD Diagnosis. Journal of Biomedical Informatics, 2024, 157, 104714. https://doi.org/10. 1016/j. jbi.2024.104714
19. Niu, K., Guo, J., Pan, Y., Gao, X., Peng, X., Li, N., Li, H. Multichannel Deep Attention Neural Networks for the Classification of Autism Spectrum Disorder Using Neuroimaging and Personal Characteristic Data. Complexity, 2020, 2020, 1-9. https://doi.org/10.1155/ 2020/1357853
20. Padmanabhan, A., Lynch, C.J., Schaer, M., Menon, V. The Default Mode Network in Autism. Biological Psy-

chiatry: Cognitive Neuroscience and Neuroimaging, 2017, 2, 476-486. https://doi.org/10.1016/j.bpsc.2017.04.004

21. Pan, J., Lin, H., Dong, Y., Wang, Y., Ji, Y. MAMF-GCN: Multi-Scale Adaptive Multi-Channel Fusion Deep Graph Convolutional Network for Predicting Mental Disorder. Computers in Biology and Medicine, 2022, 148, 105823. https://doi.org/10.1016/j.compbiomed.2022.105823
22. Tonello, L., Giacobbi, L., Pettenon, A., Scuotto, A., Cocchi, M., Gabrielli, F., Cappello, G. Crisis Behavior in Autism Spectrum Disorders: A Self- Organized Criticality Approach. Complexity, 2018, 1, 5128157. https://doi.org/ 10.1155/2018/5128157
23. Vaswani, A., Shazeer, N., Parmar, N., Uszkoreit, J., Jones, L., Gomez, A. N., Kaiser, Ł., Polosukhin, I. Attention is All You Need. Proceedings of the 31st International Conference on Neural Information Processing Systems (NIPS'17), 2017, 6000-6010.
24. Wang, Q., Li, H.-Y., Li, Y.-D., Lv, Y.-T., Ma, H.-B., Xiang, A.-F., Jia, X.-Z., Liu, D.-Q. Resting-State Abnormalities in Functional Connectivity of the Default Mode Network in Autism Spectrum Disorder: A Meta-Analysis. Brain Imaging and Behavior, 2021, 15, 2583-2592. https://doi. org/10.1007/s11682-021-00460-5
25. Wang, Y., Long, H., Bo, T., Zheng, J. Residual Graph Transformer for Autism Spectrum Disorder Prediction. Computer Methods and Programs in Biomedicine, 2024, 247, 108065. https://doi.org/10.1016/j.cmpb.2024.108065
26. Wang, Y., Long, H., Zhou, Q., Bo, T., Zheng, J. PLSNet: Position-Aware GCN-Based Autism Spectrum Disorder Diagnosis Via FC Learning and ROIs Sifting. Computers in Biology and Medicine, 2023, 163, 107184. https://doi.org/ 10.1016/j.compbiomed.2023.107184
27. Wen, G., Cao, P., Bao, H., Yang, W., Zheng, T., Zaiane, O. MVS-GCN: A Prior Brain Structure Learning-Guided Multi-View Graph Convolution Network for Autism Spectrum Disorder Diagnosis. Computers in Biology and Medicine, 2022, 142, 105239. https://doi.org/10.1016/j. compbiomed. 2022.105239
28. Xia, M., Wang, J., He, Y. BrainNet Viewer: A Network Visualization Tool for Human Brain Connectomics. PLoS ONE, 2013, 8, e68910. https://doi.org/10.1371/journal.pone. 0068910
29. Yang, X., Chen, F., Li, Z., Liu, G. Point Cloud Upsampling Network Incorporating Dynamic Graph Convolution and Multi-Head Attention. Information Technology and Control. 2024, 53, 1119-1138. https://doi.org/10.5755/j01.itc.53.4. 37310
30. Yang, X., Zhang, N., Schrader, P. A Study of Brain Networks for Autism Spectrum Disorder Classification Using Resting-State Functional Connectivity. Machine Learning with Applications, 2022, 8, 100290. https://doi. org/10.1016/j.mlwa.2022.100290
31. Zhang, J., Guo, J., Lu, D., Cao, Y. ASD-SWNet: A Novel Shared-Weight Feature Extraction and Classification Network for Autism Spectrum Disorder Diagnosis. Scientific Reports, 2024, 14, 13696. https://doi.org/10.1038/s41598-024-64299-8
32. Zhang, Z., Jin, J., Jagersand, M., Luo, J., Schuurmans, D. A Simple Decentralized Cross-Entropy Method. In Proceedings of the 36th International Conference on Neural Information Processing Systems (NIPS '22), 2022, 2644, 36495-36506.
33. Zheng, S., Zhu, Z., Liu, Z., Guo, Z., Liu, Y., Yang, Y., Zhao, Y. Multi-Modal Graph Learning for Disease Prediction. IEEE Transactions on Medical Imaging, 2022, 41, 2207-2216. https://doi.org/10.1109/TMI.2022.3159264
34. Zhuo, C., Li, G., Lin, X., Jiang, D., Xu, Y., Tian, H., Wang, W., Song, X. The Rise and Fall of MRI Studies in Major Depressive Disorder. Translational Psychiatry, 2019, 9, 1, 335. https://doi.org/10.1038/s41398-019-0680-6